Nanoscale

PAPER

View Article Online
View Journal | View Issue



Cite this: *Nanoscale*, 2025, **17**, 12361

# Electrical properties of collapsed $MoS_2$ nanotubes†

Matjaž Malok, *[a,b] Janez Jelenc [a] and Maja Remškar [a]

Molybdenum disulfide ($MoS_2$) is a promising material for future high-performance and ultra-low-power electronics. Growth from a vapor phase at chemical equilibrium enables the production of crystals possessing a relatively low density of structural defects. Besides thin $MoS_2$ flakes, $MoS_2$ nanotubes (NTs) and collapsed NTs in the shape of nanoribbons (NRs) are also synthesized in the same growth process. Here, we present the first study on the structural and electrical properties of the NRs. High resolution electron microscopy revealed a chiral structure of the NRs with no peculiarities at the inner interface where both walls are in contact. In contrast, resonant Raman spectroscopy revealed the presence of bands typical of a few layers thick $MoS_2$, suggesting that some of the layers of the NR are partially split. Contact current imaging spectroscopy (CCIS) revealed longitudinal wrinkles on the NR surface, with elevated regions found to be more conductive than the depressed areas. The edges of the NR, where molecular layers are strongly curved but not broken, exhibit varying conductivity. While some parts exhibit zero conductivity, others show much higher conductivity than the central part of the NR, suggesting an electron confinement effect. Charge injections strongly altered the NR's work function and induced changes in the NR's topography. The surface wrinkling was intensified, and the NR tended to rotate around its longitudinal axis. This rotation is explained as the reverse piezoelectric effect.

Received 20th January 2025,
Accepted 8th April 2025

DOI: 10.1039/d5nr00284b

rsc.li/nanoscale



## Introduction

The demand for ultra-low-power and high-performance computing devices continues to drive the development of electronic components. Molybdenum disulfide ($MoS_2$) exhibits favourable and promising electronic and quantum properties when transitioning from a bulk material to a two-dimensional structure.[1] $MoS_2$ is an inorganic compound in the family of transition metal dichalcogenides (TMDs), composed of molecular layers with one molybdenum (Mo) atomic layer sandwiched between two sulfur (S) atomic planes. A single molecular layer of $MoS_2$ has a thickness of ≈0.65 nm.[2] Mo and S atoms inside the S–Mo–S molecular layers are connected by covalent bonds, while interactions between the molecular layers are governed by weak van der Waals (vdW) forces. $MoS_2$ exists in various forms, including tubular hollow structures that can collapse into ribbon-like (NR) structures.[3] Among the various techniques for synthesizing $MoS_2$ nanostructures,[4] chemical vapor transport (CVT) is distinguished because it occurs near chemical equilibrium and yields products with a high degree of structural perfection.[5] Density-functional-based tight-binding (DFTB) calculations show that $MoS_2$ nanotubes (NTs) exhibit a semiconducting nature regardless of their diameter.[6] Zigzag ($n$,0) NTs possess a small direct band gap, while armchair ($n$,$n$) NTs can exhibit both direct and indirect band gaps.[6] The band gap size depends on the diameter and chirality, but remains smaller than that of bulk $MoS_2$.[6]

CVT-grown $MoS_2$ NTs, as well as those that have collapsed into NRs, have been investigated as channels in field-effect transistors, demonstrating n-type behaviour with ON/OFF current ratios exceeding $10^3$,[7] and have also been utilized as electron field emitters.[8] Due to a low density of defects, the transport properties of $MoS_2$ NTs studied at cryogenic temperatures indicate quantized single quantum-level transport.[9] Furthermore, studies have shown that $MoS_2$ NTs prepared by the CVT method can confine electromagnetic fields within their walls, leading to the appearance of whispering gallery modes (WGMs).[10] If the NTs are flattened into a NR, the degree of WGM peak splitting is expected to vary depending on the aspect ratio of the NR's cross-section. Consequently, they can be employed as optical resonators for self-radiating light, with the ability to tune the frequency at which the radiation is amplified.[11]

Despite the recent interest in $MoS_2$ monolayers and NTs, the impact of their collapse on electrical properties remains largely unexplored. Conductive atomic force microscopy

[a]*Solid State Physics Department, Jozef Stefan Institute, Ljubljana, Slovenia. E-mail: matjaz.malok@ijs.si*
[b]*Faculty of Mathematics and Physics, University of Ljubljana, Ljubljana, Slovenia*
† Electronic supplementary information (ESI) available. See DOI: https://doi.org/10.1039/d5nr00284b

(CAFM) has been used to investigate the electrical properties and Schottky barrier height at $MoS_2$ interfaces with metals,[12–15] with Si[16] and GaN,[17] as well as in the epitaxial $MoS_2$–$WSe_2$–graphene heterostructures.[18] Additionally, CAFM has been employed to probe grain boundaries in multilayer $MoS_2$ [19] and to study the current injection mechanism at the surface of $MoS_2$ thin films.[20] Charge transport properties investigated by charge injection and Kelvin probe force microscopy (KPFM) have been reported for flat $MoS_2$, including few-layered $MoS_2$ films and flakes,[21,22] and for a single $MoS_2$ NT.[23] On the other hand, extensive research has focused on carbon NTs. The effect of collapse on the atomic and electronic structure of carbon NTs has been characterized using tapping mode AFM[24] and scanning tunneling microscopy (STM).[25,26] By recording tunneling spectra at various distinct locations, researchers observed that deformation induces an electronic band gap in an otherwise metallic NT due to altered interlayer interactions.[26] Furthermore, carbon NT FET has been characterized using CAFM.[27]

Recognizing the significant implications of the collapse of the $MoS_2$ NTs for electronic applications, we investigate the electronic properties of the $MoS_2$ NRs. These structures, featuring mutually rotated walls and edges, where the S–Mo–S molecular layers remain intact but are highly curved, represent an intriguing anisotropic system. Employing STM and CAFM, we examined their electronic characteristics. Additionally, charge transport properties were studied through charge injection experiments utilizing a conductive AFM probe in STM mode for injection and KPFM for observation of work function (WF) modulation.

# Experimental

### Synthesis

$MoS_2$ was synthesized *via* a CVT reaction at 1010 K in a quartz ampoule, utilizing iodine as the transport agent. The majority of the transported material formed thin, strongly undulated flakes. On top of these $MoS_2$ flakes, the $MoS_2$ NTs grew during the last phase of the synthesis. Some of these NTs partially or fully collapsed into the shape of a NR. The proposed reason for the collapse is an obstacle that impedes longitudinal growth. To circumvent this obstacle and continue growing, the wall near the obstacle becomes deformed and approaches the opposite wall, ultimately leading to the closure of the internal hole. Such a collapsed structure is stabilized by vdW attractive interactions between both walls of the NR.[3]

### Sample preparation

The NRs (15–30 nm thick and 1–2 μm wide) were placed on a p-doped silicon substrate (Siegert Wafer) using the adhesive tape (Nitto Denko ELP BT-150E-CM) method (Fig. 1a).

### Electron microscopy

An environmental scanning electron microscope (SEM) (Quanta 650 (Thermo Fisher Scientific)) was used for the investigation of surface topography. Energy-dispersive X-ray spectroscopy (EDS) was performed with an Ultim Max 40 $mm^2$ SDD detector (Oxford Instruments). High-resolution transmission electron microscopy (HRTEM) and electron diffraction (ED) images were acquired using a JEOL ARM 200CF microscope equipped with a cold-field emission gun (FEG) as an electron source, operating at 200 kV, and featuring Cs probe correction for TEM/STEM imaging.

### Raman spectroscopy

The vibrational properties of the NTs were studied by Raman spectroscopy using a WITec Alpha 300 RS scanning confocal Raman microscope. Off-resonance measurements were conducted in backscattered geometry using a frequency-doubled Nd:YAG laser (532 nm), focused through a 100×/0.9 microscope objective, with a laser power of approximately 0.5 mW. Resonance measurements were conducted with a He:Ne laser (633 nm), focused through a 100×/0.9 microscope objective, with a laser power of approximately 2 mW. The laser power was experimentally optimized to prevent sample damage or oxidation.

### Probe microscopy

Atomic force microscopy (AFM) and Kelvin probe force microscopy (KPFM) were performed using an Omicron UHV VT-AFM system (Scienta Omicron), operating at $10^{-9}$ mbar, with the modulation voltage for KPFM applied to the tip. A

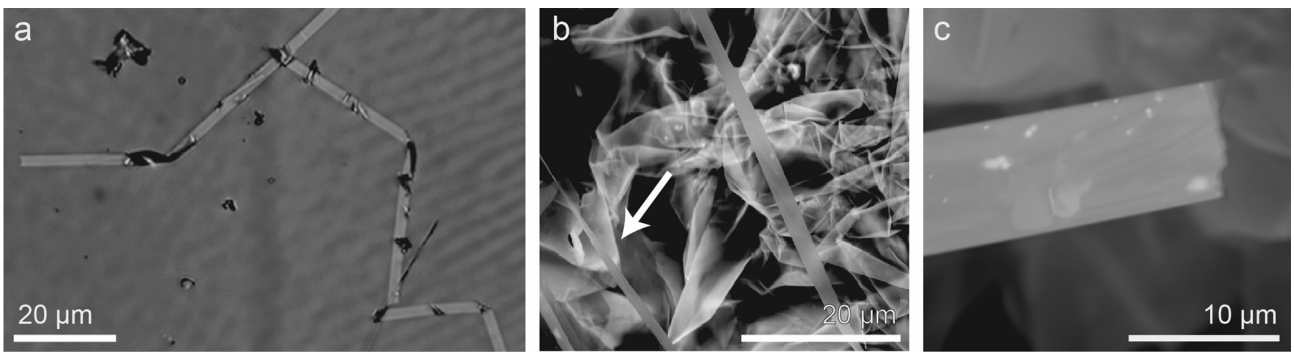


**Fig. 1** (a) Optical image of the $MoS_2$ NRs being transferred onto a p-doped silicon substrate by an adhesive tape method. (b) Backscattered SEM micrograph of as-grown $MoS_2$ NRs on top of $MoS_2$ platelets. (c) SEM image of a longitudinal end of a flat NR, 5 μm wide, with wrinkled topography.

 

silicon AFM tip coated with Pt (NSG30/Pt) was utilized. The curvature radius of a new tip, as guaranteed by the manufacturer (NT-MDT, Spectrum Instruments), was approximately 35 nm. Its resonant frequency was 320 kHz and the force constant was 40 N $m^{-1}$. The same instrument was used for contact current imaging spectroscopy (CCIS), a technique that closely resembles scanning tunneling spectroscopy (STS), with the distinction that it is performed in contact AFM (c-AFM) mode using a conductive AFM tip. Employing c-AFM, topographical data of the sample were acquired, and *I–V* measurements were conducted at specific points during the scans.

### Charge injection

Charge transport properties, carrier mobility, and charge retention were investigated through charge injections. Initially, the NR position was identified using nc-AFM, and the initial contact potential difference (CPD) values between the AFM tip and the NR, as well as between the AFM tip and the Si substrate, were recorded. The operational mode was then switched to c-AFM, enabling the AFM tip to approach the NR. The voltage applied to the tip ranged from −8 V to +8 V, the current was maintained at 333 nA, and charge injection at a given voltage lasted 6 min. Since the injection duration and current were the same for all experiments, the total injected amount of charge was also the same for all experiments. To ensure a reliable electrical contact, the tip first scanned a small section of the NR surface while a voltage was applied. The contact quality was continuously monitored by measuring the current between the NR and the tip. Once a stable contact was established, the scanning was halted, but the tip remained in contact with the NR. When a negative voltage was applied to the tip, electrons were injected from the tip to the NR. Conversely, when a positive voltage was applied to the tip, electrons flowed from the NR to the tip, injecting holes into the NR. After each injection, the tip was retracted, and the system was switched to KPFM mode to assess the CPD changes resulting from the charge injection. Extracted CPD profiles were normalized by setting the CPD of the substrate as a zero-reference level. The WF of the sample is given by $\theta_{sample} = \theta_{tip} + e{\cdot}V_{CPD}$, where $\theta_{sample}$ and $\theta_{tip}$ are the WF of the sample and the tip, respectively, $V_{CPD}$ is the CPD value, and $e$ is the elementary charge. In this context, an increase in CPD corresponds to an increase of the WF.[28] To ensure accurate analysis, the topography image tilt was corrected using the Max Flatness Tilt function in Scanning Probe Image Processor 6.7.5 software (Image Metrology). The topography images and CPD values were then compared by extracting the line profiles from the same positions on the NR to evaluate the impact of charge injection on the NR's morphology and WF relative to their initial states.

## Results and discussion

### Structural characterization

Three $MoS_2$ NRs placed on a p-doped silicon substrate are shown in Fig. 1a. All of them are twisted but not gradually as in their pristine shape. Instead, they form kinks due to being pressed during the sample transfer process and interaction with the substrate. A backscattered SEM image of pristine $MoS_2$ NRs grown on top of $MoS_2$ thin flakes is shown in Fig. 1b. The 2.6 μm wide NR, marked with an arrow, is helically twisted as a result of its chiral structure. Several μm wide NRs, such as the one in the central part of Fig. 1b, are typically not twisted because the influence of chirality on the NR shape is weakened, with strain distributed across a larger number of layers. In the vicinity of the transition from a tubular to a NR shape, the surface is wrinkled (Fig. 1c) due to the incorporated strain. The chemical composition of the NRs was studied using EDS, revealing that the Mo : S atomic ratio remains uniform across the surface, regardless of the wrinkled topography.

Structural analysis of NRs was performed using HRTEM and transmission electron diffraction (TED). Narrow NRs allow observation of the interface between both walls without making a cross-section. The NR shown in Fig. 2a is twisted along its axis. A high-resolution TEM image of the narrowest area of the NR (24 nm wide), where $MoS_2$ layers are parallel to the electron beam, reveals that the interface between both walls, composed of 18 molecular layers, is without peculiarities, making the NR appear as a single-crystal struc-

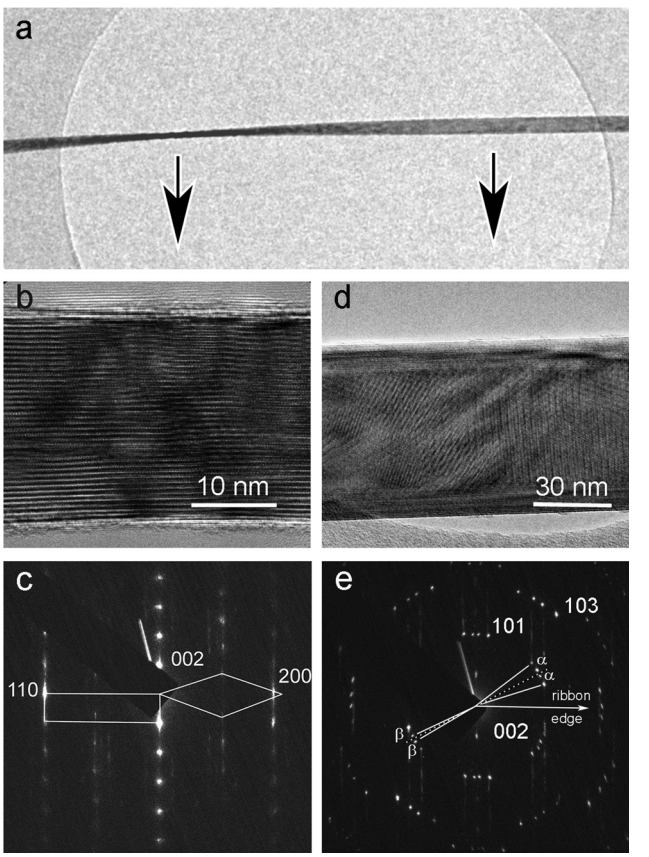


**Fig. 2** TEM images with corresponding electron diffraction patterns of a helically twisted $MoS_2$ NR (a), taken at the narrowest part (b and c) and at the widest part (d and e) in the projection view.

ture (Fig. 2b). The corresponding TED pattern (Fig. 2c) corresponds to a superposition of electrons scattered in two zone-axes: [010] and [110]. The diffraction peaks (*hkl*) in the [010] zone-axis satisfy the rule $l = \pm(2n + 1)$ that corresponds to the 2Hb polytype stacking. In the projection of the side (10*l*) reflections onto the [00*l*] axis, the spots appear exactly between (00*l*) spots.[29] The widest part of the NR, where $MoS_2$ layers in the central part are perpendicular to the electron beam, measures 65.5 nm in width. The TEM image (Fig. 2d) reveals walls with a thickness of 12 nm ± 1 nm and moiré patterns in the central part of the NR, formed by a superposition of two mutually rotated walls. Two chiral angles are identified in the electron diffraction pattern (Fig. 2e): 9.5° ($\alpha$) and 2° ($\beta$). Additionally, some wrinkles are visible in the central part of the NR.

### Raman spectroscopy

Fig. 3a shows the off-resonant (gray) and direct resonant (black) Raman spectra taken on a $MoS_2$ NR. In the off-resonant spectrum, characteristic bands of $MoS_2$ NRs are observed at 383, 409, 451, and 464 $cm^{-1}$, in agreement with previously reported results.[7,30] The main Raman bands at 383 and 409 $cm^{-1}$ correspond to the in-plane vibration of sulfur and molybdenum atoms in opposite directions ($E^1_{2g}$ mode) and to the out-of-plane vibration of sulfur atoms in opposite directions ($A_{1g}$ mode), respectively.

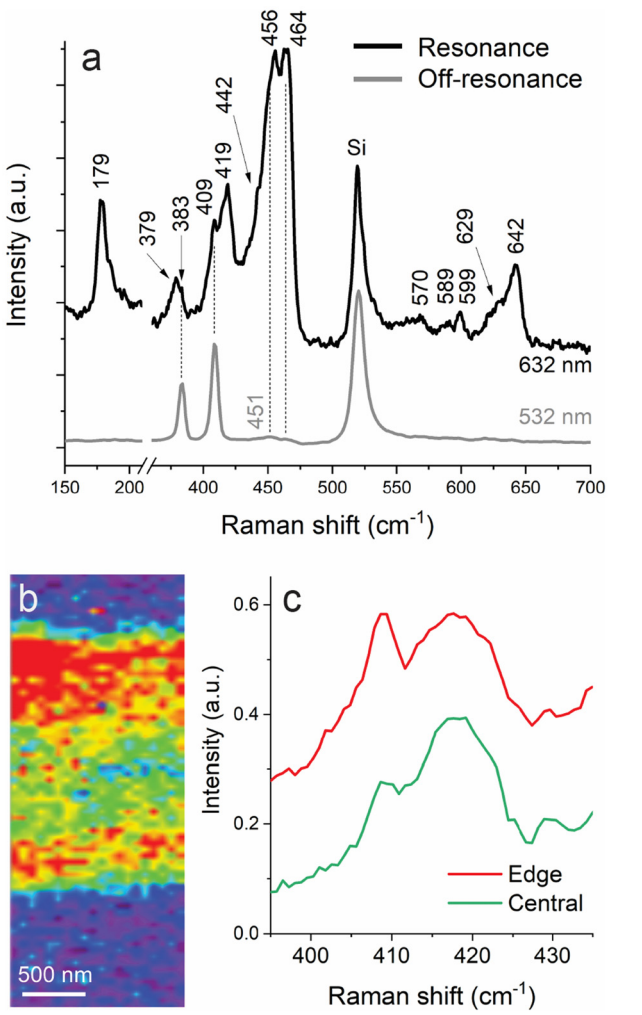


**Fig. 3** (a) Direct resonance (black) and off-resonance (grey) Raman spectra of the $MoS_2$ NR. (b) Raman mapping of the $MoS_2$ NR, shown as an intensity of a band at 409 $cm^{-1}$. (c) Enlarged Raman spectra obtained at $MoS_2$ edges (red) and the central part (green).

Direct resonant Raman scattering reveals additional bands compared to non-resonant scattering, as previously reported.[31–42] The most intensive Raman bands were observed at 179 $cm^{-1}$, 419 $cm^{-1}$, 456 $cm^{-1}$, 464 $cm^{-1}$, and 642 $cm^{-1}$. The absence of bands around 230 $cm^{-1}$ indicates a low concentration of defects in the sample.[31–35] On the low-frequency side of the $E_{2g}{}^1$ band at 383 $cm^{-1}$, its Davydov pair, the Raman-inactive $E_{1u}{}^2$ mode at 379 $cm^{-1}$, is observed. The small frequency split of the Davydov pairs indicates a weak interlayer interaction.[36,37] The intensity of the 379 $cm^{-1}$ band exceeds the intensity of the peak at 383 $cm^{-1}$. The 419 $cm^{-1}$ band was previously observed at 430 $cm^{-1}$ in $MoS_2$ single crystals,[36] and it was reported to downshift to 420 $cm^{-1}$ in nanoparticles.[32,36] This peak is attributed to a two-phonon Raman process involving the successive emission of a dispersive quasi-acoustic (QA) phonon and a dispersionless TO phonon.[36] The most intense band is observed around 460 $cm^{-1}$, which is a superposition of the two bands at 456 and 464 $cm^{-1}$.[32] In the non-resonant Raman scattering, these bands at 456 $cm^{-1}$ and 464 $cm^{-1}$ were barely visible.

The intensity of some bands varies across the NR. Raman mapping (Fig. 3b) shows an increased intensity of the band at 409 $cm^{-1}$ at the edges (red) of the NR (Fig. 3c) compared to the central area (green). Such variation in intensity between the edges and basal plane of $MoS_2$ crystals has been reported previously,[43] though using a laser with a wavelength of 785 nm.

### Probe microscopy

Probe microscopy studies were conducted on three different $MoS_2$ NRs with similar dimensions. The surface and electrical structures were analysed using c-AFM and CCIS. The AFM tip was either scanned across the entire width of the NR or focused on specific regions, such as the central flat part of a NR or its longitudinal edges.

Fig. 4a shows the CCIS images of the full width of the NR at +1.6 V, revealing distinct regions oriented parallel to the NR edge with varying conductivity. At the right-hand edge, two regions of maximum conductance ($R_{inner}$ and $R_{outer}$) are separated by a valley ($R_{middle}$), where the conductance is similar to that of the central NR ($R_{central}$). This can be seen in the cross-section profiles in Fig. 4b. A similar pattern is observed at the left edge, where two maxima ($L_{outer}$ and $L_{inner}$) are separated by a valley ($L_{middle}$).

Averaged *I*–*V* spectra for the left and right edges are shown in Fig. 4c and d, respectively. The conductance of the NR is semi-conductive and slightly higher at positive biases. It is significantly greater at the right edge compared to the left one. This difference is likely due to variations in the contact interaction between the NR and the substrate, with the right edge being more exposed to the AFM probe, thereby revealing its

 

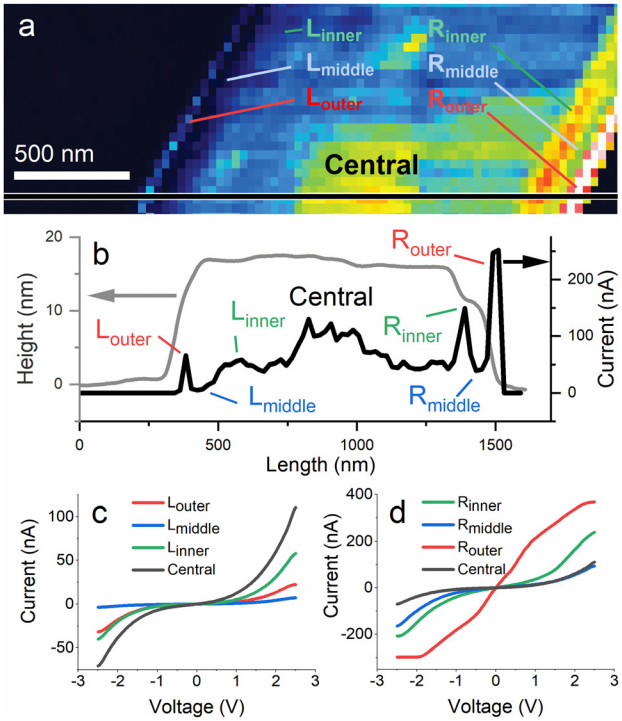


**Fig. 4** (a) CCIS images taken at +1.6 V of the full width of the $MoS_2$ NR. (b) Corresponding topography (grey) and current cross-sectional profiles (black). (c and d) Averaged *I*–*V* spectra from the left and right edges, respectively.

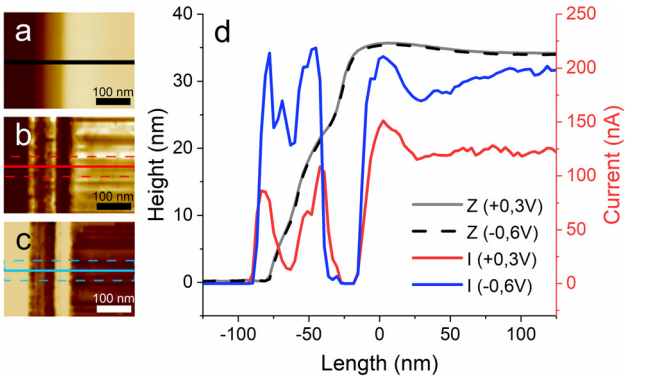


**Fig. 5** c-AFM scanning over the left edge of the $MoS_2$ NR. (a) Topography image. (b and c) Current images taken at +0.3 V and at −0.6 V, respectively. (d) Corresponding topographical and current profiles (for clarity, the absolute values of current during scanning at negative bias are shown).

electronic structuration. The local conductance at the right edge more than doubled at $R_{inner}$ and tripled at the very edge ($R_{outer}$) relative to the central region, whereas the left edge showed lower conductance compared to the central area.

The electronic properties of the NR's edge were further analysed by CAFM, applying alternating biases to the CAFM tip while simultaneously measuring the current between the sample and the tip. A c-AFM image of the NR edge is shown in Fig. 5a. The current images recorded at positive (+0.3 V) and negative (−0.6 V) voltages are shown in Fig. 5b and c, respectively. The thickness of the NR, extracted from the topography profiles (Fig. 5d, black and grey), was approximately 34 nm at both polarities, revealing a good interaction strength with the substrate, which prevented any shift of the NR due to electric force. Electronic details of the edge became visible in the current images, with cross-section profiles shown in Fig. 5d as red and blue lines for positive and negative voltages, respectively. At the border between the NR's central part and its edge (at −25 nm in Fig. 5d), a belt of zero conductivity is visible for both polarities. Between this belt and the very edge, additional structuring is observed as lines of increased conductance. Horizontal modulations (Fig. 5b and c) are artifacts of the scanning process.

The c-AFM image and the corresponding CCIS images of the NR's central part are presented in Fig. 6a and b, respectively. The surface is not completely flat but exhibits slight rippling. These ripples, with an irregular periodicity of around 100 nm, are shallow, with a height difference between the elevated and depressed areas of less than 0.5 nm. The presence of these ripples influences the local conductance such that the elevated areas have higher electric conductance than the depressed ones, as demonstrated in the CCIS image and corresponding line profiles shown in Fig. 6c. Averaged *I*–*V* profiles derived from the CCIS image are shown in Fig. 6d. Conductivity in both elevated (gold) and depressed (green) regions is greater at positive voltages. The relative difference in conductivity is more pronounced at voltages lower than −150 mV, where elevated regions exhibit 21% greater conductivity compared to the depressed areas. As the voltage increased from −150 mV to 250 mV, the relative difference in conductivity decreased linearly from 21% at −150 mV to approximately 6% at 250 mV (ESI 1†).

Some bulbs were also visible in the topography image of one $MoS_2$ NR, but they were not visible in the KFPM image. The results of a detailed investigation of these bulbs are presented in ESI 2.†

## Charge injection experiments

Before the first charge injection, nc-AFM and KPFM images were obtained (ESI 3a and b†). Both topography and Kelvin images show a shallow depression in the central part, 0.5 nm and 25 mV deep, respectively (Fig. 7, initial). Charge was injected into the NR in an area just below the presented view shown in ESI 3.† First, electrons were injected three times at −8 V bias with 40 min time delays. The first injection of electrons at −8 V already caused the surface of the NR to develop long-periodic wrinkles (ESI 3c†) and steeper sides (Fig. 7, −8 V (1)). These wrinkles were three times deeper than the ripples observed before the injections, while their periodicity ranged in the hundreds of nm. Five main wrinkle peaks were visible. The NR width at half of its thickness was reduced by approximately 7% after the first injection and did not change further with subsequent injections, whereas the average height gradually increased, reaching a 6% larger value than before the

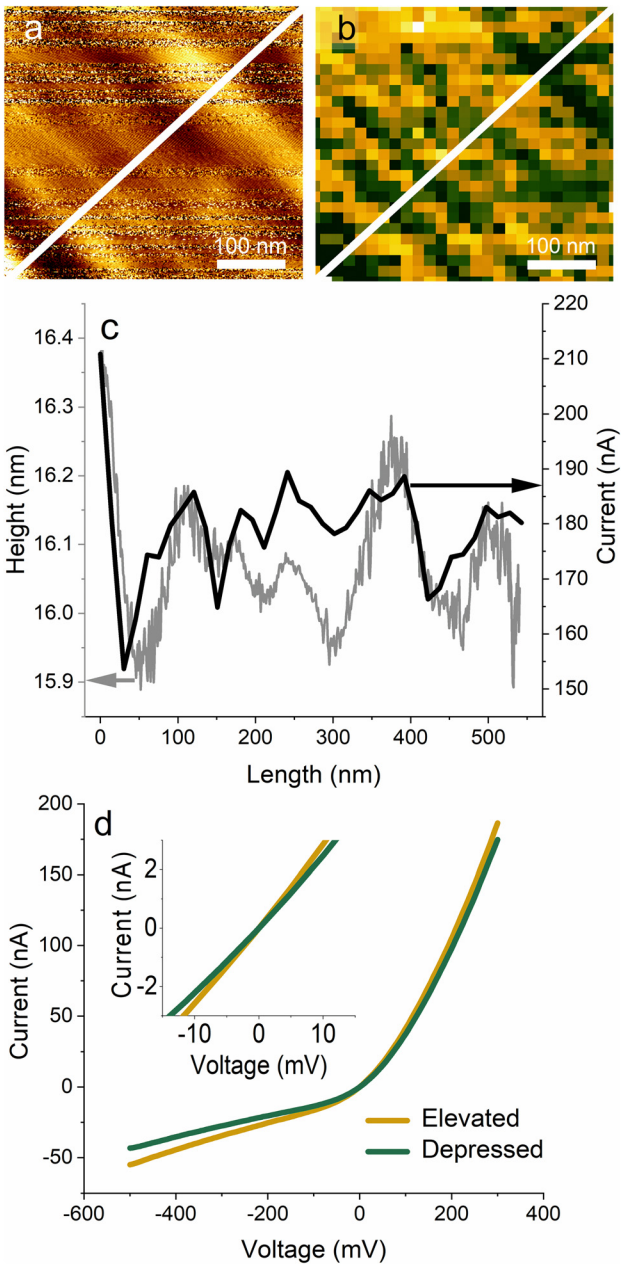


**Fig. 6** The central part of the $MoS_2$ NR. (a) c-AFM topographical image revealing a rippling surface. (b) CCIS image obtained at +0.3 V with areas of higher (gold) and lower (green) currents. (c) Corresponding line profiles. (d) *I*–*V* spectra obtained in elevated regions with higher (gold) and depressed regions with lower (green) conductance (averaged 23 and 26 spectra, respectively).

injections (Fig. 7). Simultaneously, the WF consistently decreased after each injection of electrons, as CPD dropped from ≈450 mV before the first injection to ≈350 mV after the third injection of electrons (Fig. 7). However, in the next 24 h, CPD slightly increased by approximately 30 mV.

Fig. 8 shows the result of four injections of holes at +8 V bias, performed subsequently with 40 min time delays. The nc-AFM and KPFM images of the NR before the first injection, after the last injection, and 24 h after the last injection are shown in ESI 4.† Changes in topography are mainly visible at the NR edges, which appear wider as a new belt appeared on the right-hand side of the NR after the 2nd injection, as seen in the topography profile (Fig. 8, +8 V (2)). The number of wrinkles on the NR surface decreased from 5 in the initial state to 4, with an additional one attributed to the newly occurred belt. With additional injections, it appears that the NR rotated slightly around its longitudinal axis in a clockwise direction. This is evidenced by the decrease in height of the belt on the right-hand side, which disappeared completely after the fourth injection (Fig. 8, +8 V (4)). However, during this injection, a new belt formed on the left-hand side and remained visible until the following day.

In contrast to the gradual decrease of WF with the injection of electrons, the WF did not increase monotonically with the injection of holes at +8 V bias, as one might have expected. After the first injection, the CPD decreased, while the second injection caused an increase in the CPD to a maximum value of 450 mV. A depression in the CPD profile deepened to ≈70 mV with a simultaneous increase in CPD at the NR edges. The 3rd and the 4th injections caused a decrease in CPD, while the depression in the CPD profile became less pronounced. In the next 24 h, the CPD increased, and the depression in the centre of the NR became visible again.

## Discussion

$MoS_2$ NRs were first reported as stable structures decades ago, but their structural and electronic properties have not been investigated in detail. Our TEM and TED investigations reveal that they grow in a chiral mode with at least two chiral angles. Their cross-sectional view confirms the growth mechanism, explaining their formation through the collapse of a hollow tube. The newly formed interface between the inner surfaces of both walls does not exhibit any peculiarities compared to other vdW gaps among the molecular layers. The chiral structure of pristine $MoS_2$ NTs is also preserved in the NR. Two mutually rotated walls of the NR cause an occurrence of a moiré pattern.

The overall conductivity of the NR was found to be semiconductive at room temperature and higher for positive voltages. This confirms a pristine n-type semiconducting nature of $MoS_2$,[44] but with no open gap at room temperature all over the central part of a NR. The collapse strongly curved and consequently strained the molecular layers at the NR edges, causing significant differences in conductivity in comparison with the central part. The NR edges were found to be semimetallic, which can be explained by the incorporated strain as it was theoretically predicted by E. Scalise *et al.*,[45] and experimentally demonstrated for 2D $MoS_2$ layers where moderate strain values (~2%) can already trigger an indirect bandgap transition, induce a finite charge carrier density,[46] and enhance carrier mobility.[47] From the absence of vibrational modes at 154 $cm^{-1}$, 219 $cm^{-1}$ and 327 $cm^{-1}$, it can be con-

 

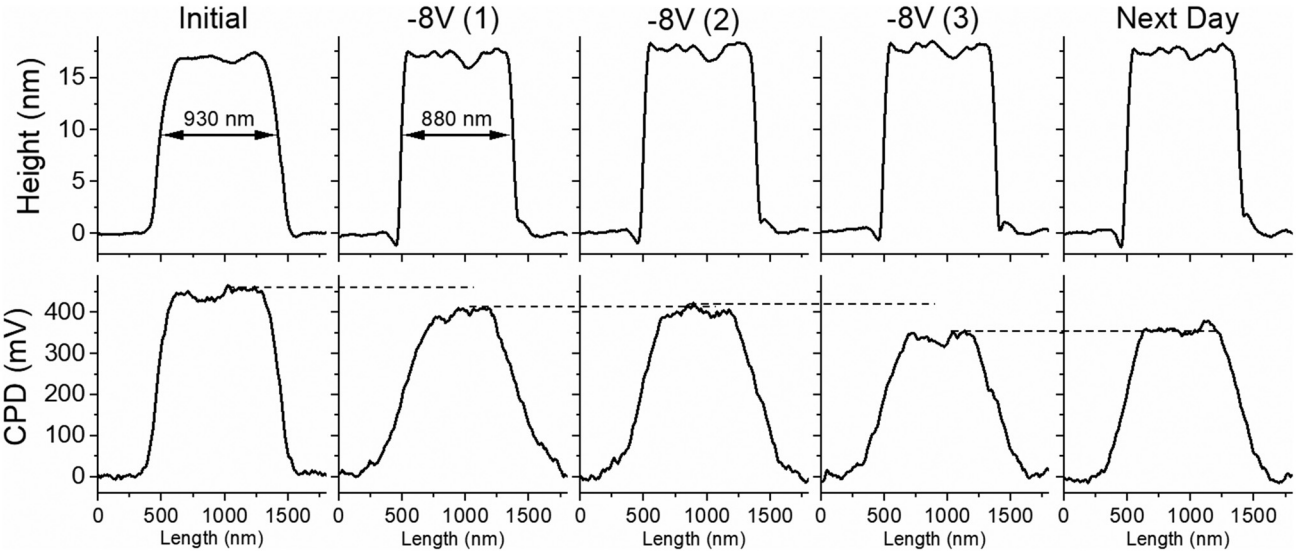


Fig. 7 Topography (top) and CPD (bottom) profiles, extracted over the NR, showing changes in topography and WF due to injection of electrons.

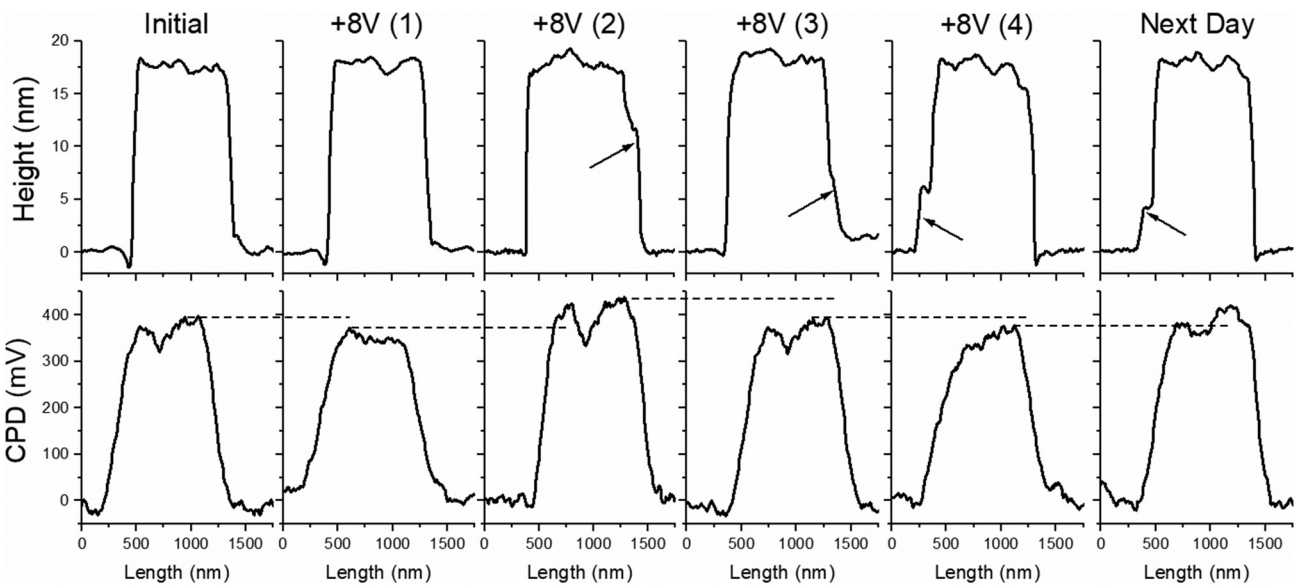


Fig. 8 Topography (top) and CPD (bottom) profiles, extracted over the NR, showing changes in topography and WF due to injection of holes.

cluded that the presence of metallic 1T-$MoS_2$ is less likely.[48] At the transition between the central part and the edges, where a strong conductance modulation was observed, some narrow belts showed zero conductance (Fig. 6d). The difference between the left and right edges can be explained by different contacts between the NR and the substrate, which can alter their electrical characteristics.[49] A relatively weak vdW contact interaction with the substrate can enable a buckling of the NR to one side influenced by a torsional strain of the chiral lattice structure or a torsional component of a reverse piezoelectric effect, which will be discussed later.[23]

All the microscopic techniques used (SEM, c-AFM and nc-AFM) revealed that the surface of the NRs is not flat but slightly rippled with a roughness of less than one molecular layer. The CCIS investigation of these ripples revealed that the elevated parts are more conductive than the depressed ones. This is in accordance with the KPFM investigation of atomically thin $MoS_2$, where space-dependent surface potential and a non-uniform charge distribution were attributed to local strain in the ripples.[50] A different differential conductivity in valleys, hills, and flat parts of $MoS_2$ monolayers (MLs), investigated by STM, was explained by bandgap changes resulting from substrate-induced local bending strain.[51] For a relatively thick $MoS_2$ NR (17 ± 1 nm) compared to an $MoS_2$ ML, interaction with the Si substrate is less likely. However, one must also consider the interaction with the second wall of a former NT

before its collapse into an NR shape. A contact between both walls in the central part of the NR must satisfy one of the possible polytypic stackings of $MoS_2$ (2H, 3R), which can induce a local strain at the interface and lead to the formation of ripples.

Besides ripples, bulbs were observed in the central part of the NR. The conductivity of these bulbs was higher than that of the surrounding flat regions, particularly at positive voltages. Distinct electronic properties of the bulbs and the flat regions between them have already been documented in collapsed carbon NTs, where the central semi-flat region maintains a finite density of states (DOS), displaying metallic behaviour, while the bulbs exhibit a bandgap opening with zero DOS, indicative of semiconductor-like characteristics.[25,52] This phenomenon is attributed to quantum confinement and charge transfer interactions between the bilayer graphene-like region and the NT-like edges, which exhibit weaker inter-wall interactions compared to the flattened region.[52]

Upon investigating charge transport properties and their retention, it was demonstrated that both negative and positive charges could be injected into the NRs, which is consistent with previous research on $MoS_2$ thin films.[21,22,53] The injected charge was trapped at the structural and electrical defects and at the interface between the NR and substrate, where a kind of 1D potential well is formed due to the different work functions of two semiconductors, forming a heterojunction. Since the 17 nm NR effectively screens charges from the $MoS_2$–$SiO_2$ interface[54] and given that $MoS_2$ exhibits significantly higher in-plane conductivity compared to interlayer conductivity, where the vdW interaction between layers acts as a tunnel barrier introducing resistance,[55] the observed change in CPD originates from electrons trapped at the surface of the NR. Taking this into account, the calculated charge density (ESI 5†) after the last injection of electrons was 0.21 mC $m^{-2}$. Injection of negative charge (electrons) decreases WF and injection of positive charge (holes) increases the NR's WF. A monotonic decrease in WF was observed with subsequent injection of electrons, whereas during injection of holes (Fig. 8), a monotonic increase in WF was not achieved. The reason for this could be the formation of new electron transport paths in the material, caused by the formation of structural defects during the charge injection.[56] Changes in work function, as well as in topography, remained stable at least for 24 h, as previously reported.[53] As $MoS_2$ is an n-type semiconductor due to electron-donating native defects,[44] it would be expected that the retention of holes would be less durable than that of electrons. However, this was not the case. This discrepancy may be attributed to charge trapping, not only at the defects but also at the potential barrier at the NR–substrate interface or between the two walls of the NR. The charge distribution on the surface was not perfectly homogeneous, as a slight depression or elevation formed in the central part. A similar but more pronounced effect was observed during charge injection into non-collapsed $MoS_2$ NTs.[23] After injection of electrons, the work function decreased in the central part of the NT, falling below that of the $MoS_2$ single crystal used as the substrate, while at the edges, trapped electrons and/or tensile strain increased the work function, making it higher than that of the substrate. The opposite trend was observed for hole injection. Furthermore, the changes in the NT's contact potential difference were much larger (400 mV) compared to the $MoS_2$ NR (100 mV). A possible reason for this is the much smaller surface area of the NT than that of the NR.

Charge injection also caused a change in the NR's shape observed as wrinkles on the surface and the rotation of the NR around its longitudinal axis. After charge injection, a very stable number (5) of wrinkles appeared oriented along the NR length. They were observed already after the first injection of electrons and did not change during subsequent injections. It is important to note that these wrinkles are not visible in KPFM images and do not affect a local work function. The wrinkling of the surface can be caused by different mechanisms. First, it is possible that the wrinkling occurred during charge injection, where the external electric field drives weakly coupled dichalcogenide layers into an unstable state, making them susceptible to mechanical exfoliation[57] and consequently leading to wrinkling. Additionally, surface wrinkling could result from charge-induced lattice deformations[58] or unevenly distributed electrons on the surface caused by Coulomb repulsion (ESI 5†). Above all, these shape changes could result from the charge injection-induced inverse piezoelectric effect, which exhibits both radial and torsional components in chiral NTs.[59] The extent of deformation depends on the diameter of individual molecular layers, meaning that different layers within the NT's wall, each with distinct circumferences and curvature energies, experience varying degrees of strain. This induces helical strain, leading to the compression of molecular layers with different radii while simultaneously causing their twisting.[23]

Indications of the reverse piezoelectric effect were observed as topographical modifications at the edges of the NR, which appeared wider due to the formation of a new belt on its right-hand side. With additional charge injections, the belt on the right-hand side diminished, while a new belt emerged on the left-hand side. This suggests that the NR underwent a clockwise rotation around its longitudinal axis. This rotational behaviour was observed twice in two different NRs and is attributed to the rotational component of the reverse piezoelectric effect, which induced rotation due to helical strain.[23] A similar phenomenon has been reported for $MoS_2$ NTs, where charge injection altered their shape by forming new shoulders on either side of the NT.[23] Additionally, it was possible to control the NT's rotation by adjusting the polarity of the injected charge, as injection of electrons induced clockwise rotation, while injection of holes caused counterclockwise rotation.

The presented results demonstrate that charge injection into $MoS_2$ NRs significantly affects their electrical properties, particularly surface potential and topography. Defect-free $MoS_2$ NTs have already been identified as promising materials for quantum and electronic devices.[7–9,11] However, device fabrication remains a challenge,[60] as electrical contacts to 2D

 

TMDCs have been a major limiting factor in achieving high device performance due to strong Fermi level pinning and high contact resistance.[61] For planar TMDCs, remarkable progress has recently been made in overcoming these barriers.[62–64] However, in the case of $MoS_2$ NTs and NRs, where reduced geometry adds further complexity, several approaches have recently been proposed to mitigate Schottky barrier formation.[60] Our study demonstrates that charge injection by the AFM tip, which mimics the effect of $MoS_2$ NR contacts with metals, alters the surface potential of $MoS_2$ NRs. Since surface potential has been reported to influence interfacial charge transfer and transport behavior in $MoS_2$–metal contacts,[65] this factor should be carefully considered when designing contacts for NRs. Additionally, the curved edges of NRs exhibit different electrical properties than the flat central region, which could be exploited for contact optimization, as edge contacts in 2D-$MoS_2$ have been shown to outperform flat surface contacts.[66] Furthermore, we observed that charge injection can alter the shape of NRs, potentially creating gaps between the NR and contact materials. This disruption may prevent the formation of a continuous crystalline interface, ultimately reducing contact quality.[60] These findings emphasize the need for further research into the electrical properties of $MoS_2$ NTs and NRs, as variations in their electrical characteristics could have a significant impact on the performance of electronic devices.

## Conclusions

In conclusion, the electrical properties of single $MoS_2$ NRs were investigated for the first time. The NRs form by a total collapse of $MoS_2$ NTs during the growth process and retain the chiral structure of the pristine nanostructures. The interface between both walls was found without peculiarities resembling a single crystal structure. However, Raman measurements revealed the presence of Raman bands typical of a few layers thick $MoS_2$, indicating that some of the NR layers are partially split and the long-range order in the stacking is disrupted. Conductivity was found to be dependent on specific locations within the NRs. While both edge regions exhibit higher conductivity than the central part of the NR, some belts with zero conductance were observed in the transition areas, suggesting a kind of electron confinement. Longitudinal wrinkles were observed on the NR surface, with elevated regions exhibiting higher conductivity than the depressed areas. The conductance of both elevated and depressed regions was higher at positive voltages than that at negative ones, consistent with the n-type semiconducting nature of $MoS_2$. Charge transport properties, mobility, and retention were studied through charge injection experiments, revealing that both injections of electrons and holes alter the NR's WF. Additionally, charge injection induced changes in the NR's topography, which could be attributed to the rotational component of the reverse piezoelectric effect in chiral structures. These findings highlight the need for further research into the electrical properties of $MoS_2$ NTs and NRs, as changes in their electrical characteristics could significantly influence the performance of electronic devices.

## Author contributions

M. M.: conceptualization, investigation, data curation, methodology, visualization, and writing – original draft; J. J.: investigation, data curation, and methodology; and M. R.: funding acquisition, supervision, methodology, and writing – review & editing.

## Data availability

All data that support the findings of this study are included within the article and in the ESI files.†

## Conflicts of interest

There are no conflicts to declare.

## Acknowledgements

This research was supported by the Slovenian Research and Innovation Agency *via* grants P1-0099 and PR-11224.

## References

1 O. Samy, S. Zeng, M. D. Birowosuto and A. El Moutaouakil, *Crystals*, 2021, **11**, 355.
2 X. Li and H. Zhu, *J. Mater.*, 2015, **1**, 33–44.
3 M. Remškar, Z. Škraba, F. Cléton, R. Sanjinés and F. Lévy, *Surf. Rev. Lett.*, 1998, **5**, 423–426.
4 U. Krishnan, M. Kaur, K. Singh, M. Kumar and A. Kumar, *Superlattices Microstruct.*, 2019, **128**, 274–297.
5 M. Remškar, *Adv. Mater.*, 2004, **16**, 1497–1504.
6 G. Seifert, H. Terrones, M. Terrones, G. Jungnickel and T. Frauenheim, *Phys. Rev. Lett.*, 2000, **85**, 146–149.
7 S. Fathipour, *et al.*, *Appl. Phys. Lett.*, 2015, **106**, 022114.
8 R. Ławrowski, L. Pirker, K. Kaneko, H. Kokubo, M. Bachmann, T. Ikuno, M. Remškar and R. Schreiner, *J. Vac. Sci. Technol., B:Nanotechnol. Microelectron.:Mater., Process., Meas., Phenom.*, 2020, **38**, 032801.
9 R. T. K. Schock, J. Neuwald, W. Möckel, M. Kronseder, L. Pirker, M. Remškar and A. K. Hüttel, *Adv. Mater.*, 2023, **35**, 2209333.
10 D. R. Kazanov, *et al.*, *Appl. Phys. Lett.*, 2018, **113**, 101106.
11 I. A. Eliseyev, *et al.*, *Adv. Opt. Mater.*, 2023, **11**, 2202782.
12 Y. Son, Q. H. Wang, J. A. Paulson, C.-J. Shih, A. G. Rajan, K. Tvrdy, S. Kim, B. Alfeeli, R. D. Braatz and M. S. Strano, *ACS Nano*, 2015, **9**, 2843–1855.

13 P. Bampoulis, R. van Bremen, Q. Yao, B. Poelsema, H. J. W. Zandvliet and K. Sotthewes, *ACS Appl. Mater. Interfaces*, 2017, **9**, 19278–19286.
14 F. Giannazzo, *et al.*, *ACS Appl. Mater. Interfaces*, 2017, **9**, 23164–23174.
15 F. Giannazzo, M. Bosi, F. Fabbri, E. Schilirò, G. Greco and F. Roccaforte, *Phys. Status Solidi RRL*, 2019, **14**, 1900393.
16 A. Alhammadi, W. Alnaqbi, J. Ashraf, A. Rezk and A. Nayfeh, *ECS Trans.*, 2021, **104**, 17–19.
17 D. Ruzmetov, *et al.*, *ACS Nano*, 2016, **10**, 3580–3588.
18 Y.-C. Lin, *et al.*, *Nat. Commun.*, 2015, **6**, 7311.
19 J. Ludwig, A. N. Mehta, M. Mascaro, U. Celano, D. Chiappe, H. Bender, W. Vandervorst and K. Paredis, *Nanotechnology*, 2019, **30**, 285705.
20 F. Giannazzo, G. Fisichella, A. Piazza, S. Di Franco, I. P. Oliveri, S. Agnello and F. Roccaforte, *Mater. Sci. Semicond. Process.*, 2016, **42**, 174–178.
21 G. Hao, Z. Huang, Y. Liu, X. Qi, L. Ren, X. Peng, L. Yang, X. Wei and J. Zhong, *AIP Adv.*, 2013, **3**, 042125.
22 R. Xu, *et al.*, *Nanotechnology*, 2018, **29**, 355701.
23 M. Remškar, J. Jelenc, N. Czepurnyi, M. Malok, L. Pirker, R. Schreiner and A. K. Hüttel, *Nanoscale Adv.*, 2024, **6**, 4075–4081.
24 M.-F. Yu, T. Kowalewski and R. S. Ruoff, *Phys. Rev. Lett.*, 2001, **86**, 87–90.
25 C. E. Giusca, Y. Tison and S. R. P. Silva, *Phys. Rev. B: Condens. Matter Mater. Phys.*, 2007, **76**, 035429.
26 C. E. Giusca, Y. Tison and S. R. P. Silva, *Nano Lett.*, 2008, **8**, 3350–3356.
27 L. Rispal, T. Ruland, Y. Stefanov, F. Wessely and U. Schwalke, *ECS Trans.*, 2006, **3**, 441–448.
28 S. Sadewasser and T. Glatzel, *Kelvin Probe Force Microscopy*, Springer Berlin, Heidelberg, 2012.
29 M. Remškar, Z. Škraba, C. Ballif, R. Sanjinés and F. Lévy, *Surf. Sci.*, 1999, **433–435**, 637–641.
30 M. Viršek, A. Jesih, I. Milošević, M. Damnjanović and M. Remškar, *Surf. Sci.*, 2007, **601**, 2868–2872.
31 N. T. McDevitt, J. S. Zabinski, M. S. Donley and J. E. Bultman, *Appl. Spectrosc.*, 1994, **48**, 733–736.
32 G. L. Frey, R. Tenne, M. J. Matthews, M. S. Dresselhaus and G. Dresselhaus, *Phys. Rev. B:Condens. Matter Mater. Phys.*, 1999, **60**, 2883.
33 S. Mignuzzi, A. J. Pollard, N. Bonini, B. Brennan, I. S. Gilmore, M. A. Pimenta, D. Richards and D. Roy, *Phys. Rev. B:Condens. Matter Mater. Phys.*, 2015, **91**, 195411.
34 B. R. Carvalho, Y. Wang, S. Mignuzzi, D. Roy, M. Terrones, C. Fantini, V. H. Crespi, L. M. Malard and M. A. Pimenta, *Nat. Commun.*, 2017, **8**, 14670.
35 N. B. Shinde and S. K. Eswaran, *J. Phys. Chem. Lett.*, 2021, **12**, 6197–6202.
36 T. Sekine, K. Uchinokura, T. Nakashizu, E. Matsuura and R. Yoshizaki, *J. Phys. Soc. Jpn.*, 1984, **53**, 811–818.
37 D. Kumar, B. Singh, R. Kumar, M. Kumar and P. Kumar, *Nanotechnology*, 2021, **32**, 285705.
38 J. M. Chen and C. S. Wang, *Solid State Commun.*, 1974, **9**, 857–860.
39 A. M. Stacy and D. T. Hodul, *J. Phys. Chem. Solids*, 1985, **46**, 405–409.
40 H. Li, Q. Zhang, C. C. R. Yap, B. K. Tay, T. H. T. Edwin, A. Olivier and D. Baillargeat, *Adv. Funct. Mater.*, 2012, **22**, 1385–1390.
41 B. Chakraborty, H. S. S. R. Matte, A. K. Sood and C. N. R. Rao, *J. Raman Spectrosc.*, 2012, **44**, 92–96.
42 K. Gołasa, M. Grzeszczyk, R. Bożek, P. Leszczyński, A. Wysmołek, M. Potemski and A. Babinski, *Solid State Commun.*, 2014, **197**, 53–56.
43 S. J. Brooke and M. R. Waterland, *J. Phys. Chem. C*, 2022, **126**, 12592–12602.
44 R. Dagan, Y. Vaknin, A. Henning, J. Y. Shang, L. J. Lauhon and Y. Rosenwaks, *Appl. Phys. Lett.*, 2019, **114**, 101602.
45 E. Scalise, M. Houssa, G. Pourtois, V. Afanas'ev and A. Stesmans, *Nano Res.*, 2012, **5**, 43–48.
46 J. Pető, *et al.*, *npj 2D Mater. Appl.*, 2019, **3**, 39.
47 H. Shi, H. Pan, Y.-W. Zhang and B. I. Yakobson, *Phys. Rev. B:Condens. Matter Mater. Phys.*, 2013, **87**, 155304.
48 N. H. Attanayake, *et al.*, *ACS Energy Lett.*, 2018, **3**, 7–13.
49 J. S. Soares, *et al.*, *Nano Lett.*, 2010, **10**, 5043–5048.
50 S. Luo, G. Hao, Y. Fan, L. Kou, C. He, X. Qi, C. Tang, J. Li, K. Huang and J. Zhong, *Nanotechnology*, 2014, **26**, 105705.
51 B. G. Shin, G. H. Han, S. J. Yun, H. M. Oh, J. J. Bae, Y. J. Song, C. Park and Y. H. Lee, *Adv. Mater.*, 2016, **28**, 9378–9384.
52 A. Impellizzeri, P. Briddon and C. P. Ewels, *Phys. Rev. B*, 2019, **100**, 115410.
53 R. Sanikop, N. Arya, V. Balakrishnan and C. Sudakar, *J. Phys. Chem. C*, 2021, **125**, 12155–12165.
54 A. Castellanos-Gomez, E. Cappelluti, R. Roldán, N. Agraït, F. Guinea and G. Rubio-Bollinger, *Adv. Mater.*, 2013, **25**, 899–903.
55 S. Das and J. Appenzeller, *Nano Lett.*, 2013, **13**, 3396–3402.
56 M. Gu, M. Han and S. Kim, *Curr. Appl. Phys.*, 2024, **57**, 20–25.
57 E. J. G. Santos and E. Kaxiras, *ACS Nano*, 2013, **7**, 10741–10746.
58 A. Singh, G. Sharma, B. P. Singh and P. Vasa, *J. Phys. Chem. C*, 2019, **123**, 17943–17950.
59 N. Sai and E. J. Mele, *Phys. Rev. B:Condens. Matter Mater. Phys.*, 2003, **68**, 241405.
60 R. T. K. Schock, *et al.*, *Phys. Status Solidi B*, 2024, **262**, 2400366.
61 C. Kim, *et al.*, *ACS Nano*, 2017, **11**, 1588–1596.
62 P.-C. Shen, *et al.*, *Nature*, 2021, **593**, 211–217.
63 W. Li, *et al.*, *Nature*, 2023, **613**, 274–279.
64 S. Das, H.-Y. Chen, A. V. Penumatcha and J. Appenzeller, *Nano Lett.*, 2013, **13**, 100–105.
65 M. Li, *et al.*, *Nanotechnology*, 2020, **31**, 395713.
66 D. S. Schulman, A. J. Arnold and S. Das, *Chem. Soc. Rev.*, 2018, **47**, 3037–3058.

 